Check for updates

Pyridyl-containing graphdiyne stabilizes sub-2 nm ultrasmall copper nanoclusters for the electrochemical reduction of CO_2†

Hao Dai,[a] Haiyuan Zou,[a] Tao Song,[a] Lei Gao,[b] Shuting Wei,[a] Hong Liu,[a] Huatian Xiong, [ID][a] Changshui Huang[c] and Lele Duan [ID] *[a]

Developing novel carbonaceous materials with definite chemical structures is conducive to understanding structure–property relationships and expanding their applications in supported metal catalysts. Herein, a brand-new pyridine-substituted graphdiyne (**Py-GDY**) is synthesized through the cross-coupling of 1,3,5-triethynyl-2,4,6-tris(4-pyridyl)benzene, and further applied as a promising carrier in electrocatalysis. Thanks to the precisely introduced pyridyl groups, strong metal–support interaction between the confined Cu species and **Py-GDY** is desirably obtained, resulting in uniformly dispersed Cu sub-nano-clusters (<2 nm) (**Py-GDY-Cu**). Conversely, the Cu size increased dramatically when the pyridyl group of **Py-GDY** was replaced by the phenyl group (**Ph-GDY-Cu**). In a proof-of-concept demonstration of the electrochemical CO_2 reduction reaction, **Py-GDY-Cu** is found to produce CH_4 preferentially to **Ph-GDY-Cu**, owing to the favorable sub-nanocluster size. As a result, an optimum CH_4 faradaic efficiency of 58% is achieved on **Py-GDY-Cu**, which shows a 1.6-fold enhancement compared with that of **Ph-GDY-Cu**. This work broadens the scope of carbonaceous materials for rational metal species immobilization toward efficient catalysis.

Introduction

Catalysis not only plays a vital role in the chemical industry but also attracts great attention in the field of fundamental research. Heterogeneous metal catalysts are widely used in diverse heterogeneous catalysis processes. Their supporting materials often determine the performance of metal catalysts by regulating their shapes, morphologies, sizes, and chemical states.[1–3] Carbonaceous materials are a family of supporting materials commonly used in the energy-related research field, and tremendous effort has been devoted to expanding the library of carbonaceous materials.[4,5] Heteroatom-doped carbon materials provide a representative platform for supporting metal catalysts and increasing the dispersion of metal species through strong metal–support interaction (MSI), which is expected to affect the catalytic activity.[6–8] Nevertheless, the current doping

strategies have long been championed by hydrothermal or high-temperature calcination treatment, in which the dopant types and the homogeneity of heteroatoms in carbon materials are difficult to control, putting obstacles in the way of understanding the structure–property relationships.[9,10] Hence, developing heteroatom-doped carbon materials with well-defined chemical structures is highly desirable and remains a challenge in the controllable synthesis of carbon-supported metal catalysts.

Graphdiyne (GDY) has emerged as a new two-dimensional (2D) carbon allotrope prepared *via* the cross-coupling reaction of hexaethynylbenzene.[11] With a conjugated structure composed of benzene rings and diacetylenic linkages (–C≡C–C≡C–), GDY provides defined and uniform anchoring sites for metal atoms.[12–14] A series of single-atom catalysts like Fe, Ni, Cu, Mo, Pd, Pt, Ru, Rh *etc.* has been synthesized on GDY.[12–20] MoO_3 nanoparticles, CuO nanoclusters, and oxidized iridium quantum dots are also successfully supported on GDY.[21–23] The metal atoms are stabilized by the interaction between the d orbitals of metal atoms and the π/π* orbitals of carbon–carbon triple bonds (–C≡C–). In addition, taking advantage of the bottom-up synthetic strategy, tens of GDY analogues with desired structures have been realized by precisely introducing heteroatoms (B, N, and S) or functional groups (–F, –Cl, and –CN) into the corresponding monomers.[24–29] This makes GDY analogues an ideal platform for the precise synthesis of doped carbon materials to support metal catalysts. By the rational

[a]*Department of Chemistry and Shenzhen Grubbs Institute, Southern University of Science and Technology, Shenzhen 518055, P. R. China.*
E-mail: duanll@sustech.edu.cn
[b]*National Laboratory of Solid State Microstructures (NLSSM), Jiangsu Key Laboratory of Artificial Functional Materials, College of Engineering and Applied Sciences, Nanjing University, Nanjing, 210093, China*
[c]*Beijing National Laboratory for Molecular Sciences, Organic Solids Laboratory, Institute of Chemistry, Chinese Academy of Sciences, Beijing 100190, China*
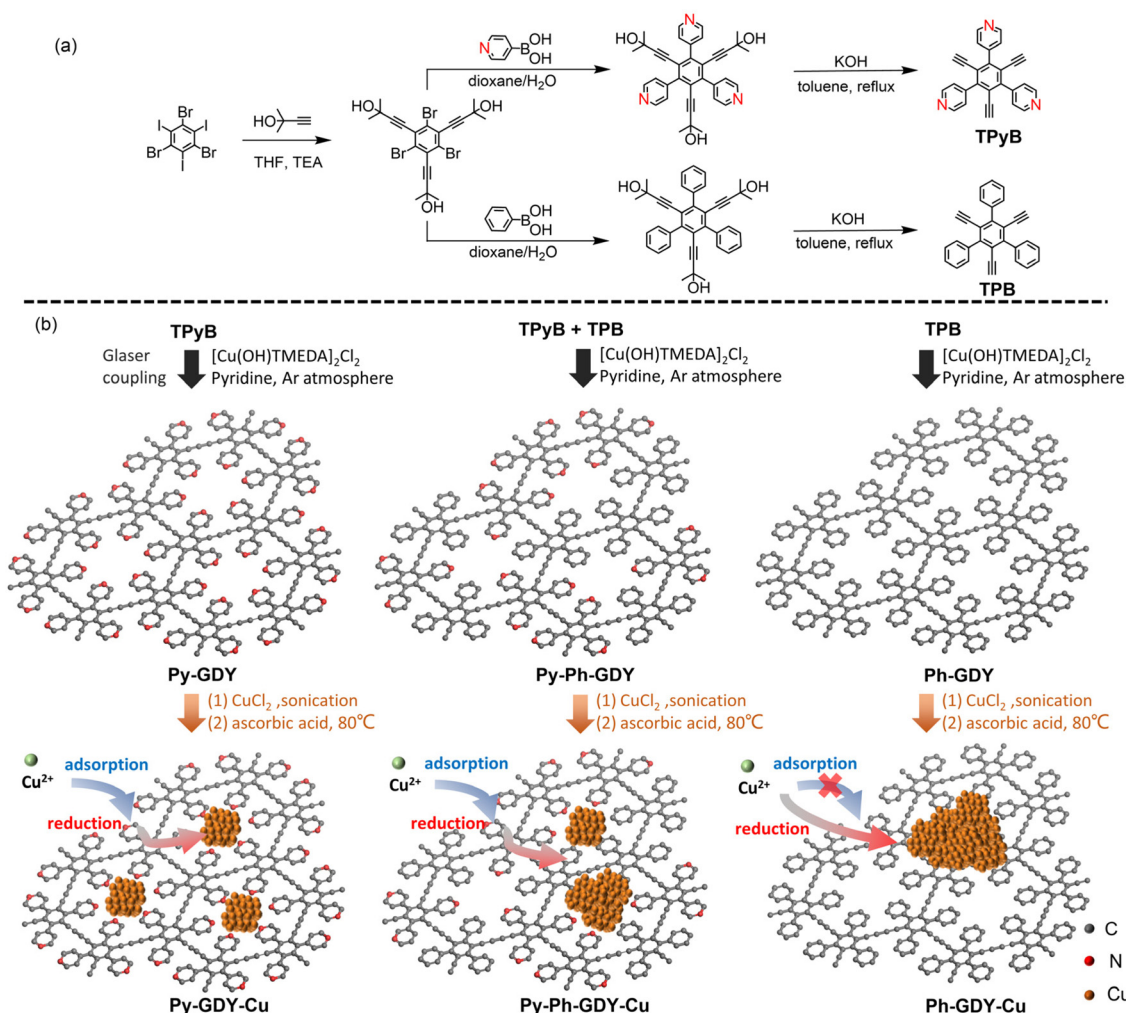†Electronic supplementary information (ESI) available. See DOI: https://doi.org/10.1039/d2qi02671f

This journal is © the Partner Organisations 2023

Inorg. Chem. Front., 2023, **10**, 2189–2196 | **2189**

Fig. 1 (a) Synthetic diagram of **TPyB** and **TPB**. (b) Schematic illustration for the preparation of **Py-GDY**, **Py-Ph-GDY**, **Ph-GDY**, **Py-GDY-Cu**, **Py-Ph-GDY-Cu**, **Ph-GDY-Cu**.

design of GDY analogues with functional groups, the MSI could be readily manipulated, which may in turn affect the sizes, morphologies, and chemical states of the supported metal catalysts.

Pyridyl groups have been widely used as coordinating ligands in various metal complexes.[30] Adopting the synthetic strategy of GDY, pyridyl groups could be uniformly incorporated into the 2D network of a GDY analogue. The pyridyl groups on the GDY analogue may play a pivotal role in the dispersion of metal atoms *via* strong metal–nitrogen interaction, thus facilitating the construction of nanosized metal catalysts.

Herein, a new pyridine-substituted GDY (**Py-GDY**; Fig. 1) is successfully synthesized *via* the cross-coupling reaction of 1,3,5-triethynyl-2,4,6-tris(4-pyridyl)benzene (**TPyB**; Fig. 1). Owing to the merits of the introduced pyridyl group, the strong interaction between the Cu species and **Py-GDY** leads to the formation of uniformly distributed sub-2 nm ultrasmall Cu clusters (**Py-GDY-Cu**; Fig. 1). As a comparison, large and uneven Cu nanoparticles were obtained on the other two GDYs, **Py-Ph-GDY** and **Ph-GDY** (see their structures in Fig. 1)

with a half content of pyridyl groups and without pyridine groups, respectively. In the electrochemical CO_2 reduction reaction, **Py-GDY-Cu** showed the highest faradaic efficiency of 58% for CH_4 at −1.0 V *vs.* a reversible hydrogen electrode (RHE) in 1.0 M KOH, surpassing that of the uneven Cu nanoparticles on **Py-Ph-GDY** and **Ph-GDY**. The favorable selectivity for CO_2-to-CH_4 conversion over **Py-GDY-Cu** is due to the ultrasmall size of the Cu catalyst originating from the presence of coordinating pyridyl groups in the GDY material. The present work not only broadens the scope of the GDY library but also highlights a compelling support material to immobilize metal catalysts toward improved catalysis.

Results and discussion

Synthesis and characterization

TPyB was prepared from 1,3,5-tribromo-2,4,6-triiodobezene in three steps: (i) the Sonogashira reaction; (ii) the Suzuki coupling reaction; and (iii) the base-promoted deprotection reac-

tion. The synthetic procedures are shown in Fig. 1a. All these compounds were thoroughly characterized using ^{1}H-NMR, ^{13}C-NMR spectroscopy, and high-resolution mass spectroscopy (Fig. S1–S10†). Using the Cu-catalyzed Glaser coupling reaction of **TPyB**, **Py-GDY** was produced with a porous framework and evenly distributed pyridyl groups, as shown in Fig. 1b. The transmission electron microscopy (TEM) image of **Py-GDY** (Fig. 2a) reveals a lamellar morphology of **Py-GDY**. Elements of C and N were uniformly distributed, as depicted by the energy dispersive spectroscopy (EDS) mapping images. The X-ray diffraction (XRD) pattern in Fig. S11† displays a broad peak at 21° assigned to the in-plane periodicity, indicating that **Py-GDY** is amorphous but still shows 2D ordering.[31]

The structure of **Py-GDY** was further investigated by the Fourier transform infrared spectroscopy (FTIR), Raman spectroscopy, and X-ray photoelectron spectroscopy (XPS). By comparison of the FTIR spectra of **TPyB** and **Py-GDY** (Fig. 2b), two IR bands at 3290 and 2094 cm^{-1} are exclusively observed for **TPyB** but not for **Py-GDY**, and these two bands are respectively due to the C–H stretching vibration of C≡C–H and the C≡C stretching vibration.[26] Apparently, the terminal acetylenic groups of **TPyB** are converted to, in principle, the diacetylenic linkages *via* the Glaser coupling reaction, leading to the formation of **Py-GDY**. The Raman spectrum (Fig. 2c) of **Py-GDY** displays four bands at 1344, 1546, 1602, and 2185 cm^{-1}. The band at 2185 cm^{-1} is attributed to the stretching vibration of conjugated diyne links (–C≡C–C≡C–),[11] verifying the cross-coupling of the terminal acetylenic groups. For XPS analysis, the C 1s peak of **Py-GDY** (Fig. 2d) is deconvoluted into four peaks of C=C at 284.5 eV, C≡C at 285.2 eV, C=N at 285.5 eV,

and C–O at 286.7 eV. The N 1s spectrum of **Py-GDY** (Fig. 2e) depicts only one peak at 398.7 eV, assigned to the N atom of pyridyl groups.[9] All the results above are in good agreement with the proposed structure of **Py-GDY**.

Pyridyl groups are widely used in coordination chemistry for their high tendency to form metal complexes.[30] With its porous structure and abundant pyridyl groups, **Py-GDY** can be a proper support for metal catalysts. To systematically examine the effects of pyridyl groups on stabilizing metal catalysts, we also synthesized another two GDY analogues, **Py-Ph-GDY** and **Ph-GDY**, as shown in Fig. 1b. **Ph-GDY** was prepared by the coupling of 1,3,5-triethynyl-2,4,6-triphenyl-benzene (**TPB**) according to the literature method.[32] Compared with **Py-GDY**, all the pyridyl groups were replaced by phenyl groups in **Ph-GDY**. To further tune the content of pyridyl groups, a mixture of **TPyB** and **TPB** with a molar ratio of 1 : 1 was used to produce **Py-Ph-GDY**. **Ph-GDY** and **Py-Ph-GDY** were also characterized by FTIR, Raman, and XPS (Fig. S12–S15†). The elemental analysis results show the C/N atomic ratios are 7.7 and 16.6 for **Py-GDY** and **Py-Ph-GDY**, which are close to the values of 9 and 19 calculated from their ideal chemical structures.

After preparing these three GDY analogues, the supported Cu nanocatalysts were further synthesized to investigate the effect of the pyridyl group on the size distribution of the Cu catalysts. In general, **Py-GDY**, **Py-Ph-GDY**, and **Ph-GDY** were respectively dispersed in a CuCl$_2$ solution by sonication, and then ascorbic acid was added to reduce Cu^{2+} into Cu nanoclusters/nanoparticles.[33] The resulting products are accordingly named **Py-GDY-Cu**, **Py-Ph-GDY-Cu**, and **Ph-GDY-Cu**. According to the EDS spectra (Fig. S16†), Cu is successfully incorporated into **Py-GDY-Cu**, **Py-Ph-GDY-Cu**, and **Ph-GDY-Cu**. But the morphologies of Cu change over the three substrates due to their different MSI, as shown schematically in Fig. 3a. No Cu particles are observed in the TEM image of **Py-GDY-Cu** (Fig. 3b). The aberration-corrected high-angle annular dark-field scanning transmission electron microscopy (HAADF-STEM) image (Fig. 3c) verifies that Cu nanoclusters with sizes smaller than 2 nm are well distributed throughout the **Py-GDY** support, in line with the EDS spectrum and maps of C, N, and Cu shown in Fig. S16† and Fig. 3d. For **Py-Ph-GDY-Cu**, Cu nanoparticles with sizes of about 10 nm (circled in red in Fig. 3e) are found; besides, Cu nanoclusters with sizes around 1–2 nm are also present on the surface of **Py-Ph-GDY-Cu** as revealed by the aberration-corrected HAADF-STEM image (Fig. 3f). In contrast, the TEM image (Fig. 3h) and the HAADF-STEM image (Fig. 3i) of **Ph-GDY-Cu** disclose the presence of Cu nanoparticles around 100 nm. The distribution of the Cu element is not even as shown in the EDS image of Cu (Fig. 3j). According to the inductively coupled plasma atomic emission spectrometry measurements, the weight percent of Cu was 4.3 wt%, 2.7 wt%, and 2.0 wt% for **Py-GDY-Cu**, **Py-Ph-GDY-Cu**, and **Ph-GDY-Cu** respectively. Both high loading and uniform distribution of Cu nanoclusters are achieved using **Py-GDY** as the support. These phenomena arise from the fact that pyridyl groups on **Py-GDY-Cu** can adsorb Cu^{2+} and provide abundant anchoring sites for the nucleation and growth of Cu
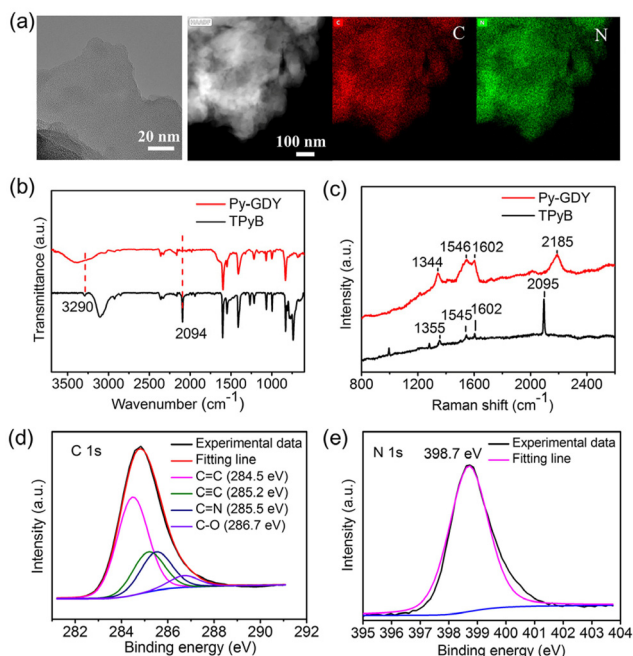

Fig. 2 (a) TEM and EDS mapping images of **Py-GDY**. (b) FTIR spectra of **Py-GDY** and **TPyB**. (c) Raman spectra of **Py-GDY** and **TPyB**. (d) C 1s XPS spectrum, and (e) N 1s XPS spectrum of **Py-GDY**.
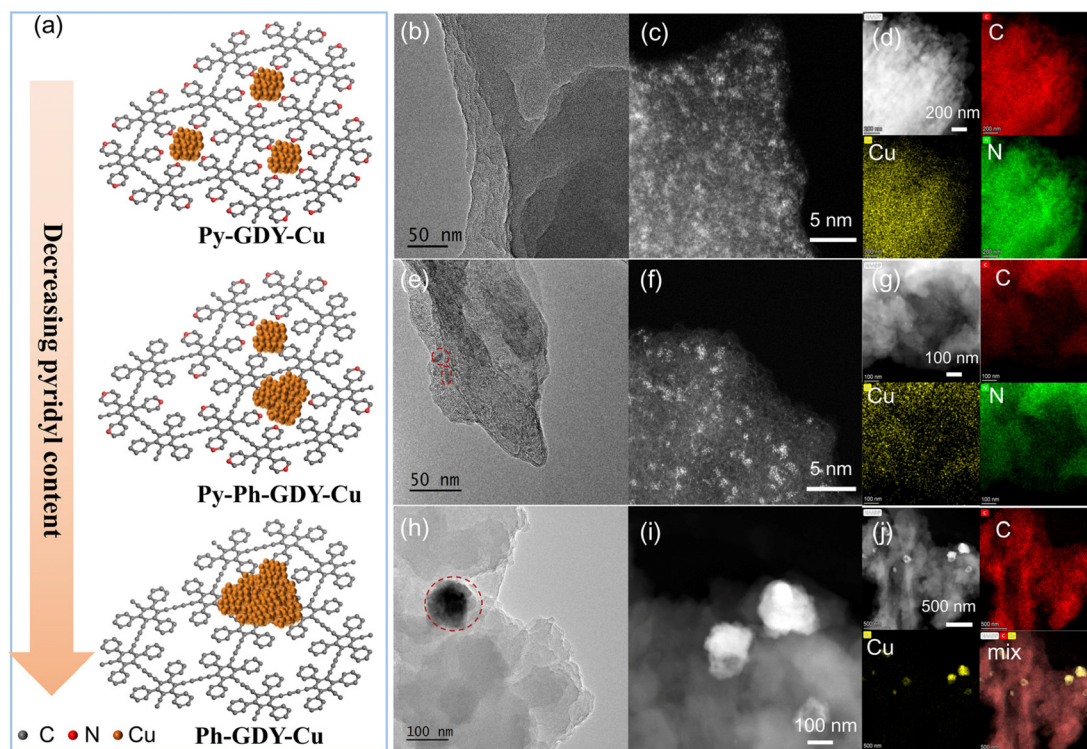
Fig. 3 (a) Schematic illustration of **Py-GDY-Cu**, **Py-Ph-GDY-Cu**, and **Ph-GDY-Cu**. (b) TEM image, (c) aberration-corrected HAADF-STEM image, and (d) EDS mapping images of **Py-GDY-Cu**. (e) TEM image, (f) aberration-corrected HAADF-STEM image, and (g) EDS mapping images of **Py-Ph-GDY-Cu**. (h) TEM image, (i) HAADF-STEM image, and (j) EDS mapping images of **Ph-GDY-Cu**.

nanoclusters. Since phenyl groups are not able to coordinate with Cu atoms, the regular structure composed of both pyridyl and phenyl groups shows a decreased ability to control the size of Cu on the **Py-Ph-GDY-Cu**. Due to the poor interaction between **Ph-GDY** and Cu, Cu easily aggregates into large nanoparticles. The XRD measurement was used to determine the structures of these three samples. In Fig. S17,† no peak of Cu is detected in the XRD patterns of **Py-GDY-Cu** and **Py-Ph-GDY-Cu**, mainly due to the rather small sizes of amorphous Cu nanoclusters.[13,19] **Ph-GDY-Cu** shows three diffraction peaks at 36.49°, 43.25° and 50.37°, due to the (111) crystal plane of Cu_2O and the (111), (200) crystal planes of metallic Cu. The existence of Cu_2O is due to the oxidation of Cu atoms under an ambient atmosphere.[33]

Further insights into the structural and electronic information on the three samples were obtained from the XPS measurements. In Fig. 4a, the characteristic peaks of C 1s and Cu 2p can be found in all three samples, and only **Py-GDY-Cu** and **Py-Ph-GDY-Cu** possess the signal of N 1s. As shown in Fig. 4b, the Cu $2p_{3/2}$ peaks around 932.9 eV and Cu $2p_{1/2}$ peaks around 952.7 eV in the Cu 2p XPS spectra are associated with Cu^0 or Cu^+.[34] No satellite peaks of Cu^{2+} are observed. The Cu LMM Auger spectra of these samples are shown in Fig. 4c. **Py-GDY-Cu** displays the most dominant Cu^+ peak, while **Ph-GDY-Cu** has the largest fraction of Cu^0.[34] This may result from the fact that small Cu nanoclusters are more easily oxidized or that Cu atoms coordinated with pyridyl groups are prone to

oxidation. The N 1s spectra in Fig. 4d demonstrate the interaction between the pyridyl groups and Cu atoms. The peak at 398.7 eV is attributed to the N 1s peak of free pyridyl groups of **Py-GDY**. After decorating Cu nanoclusters or nanoparticles on **Py-GDY** and **Py-Ph-GDY**, a new peak at 399.9 eV appears, indicating that a part of the pyridyl groups coordinates with Cu atoms, leading to a shift in the N 1s peak in the higher energy direction.

Electrochemical reduction of CO_2

The electrochemical reduction of CO_2 has emerged as a promising method for CO_2 conversion. Cu materials show a unique capability of catalyzing the electrochemical conversion of CO_2 to various hydrocarbons and alcohols.[35] Improved activity and selectivity of Cu catalysts toward specific products is in high demand. Previous studies show that the "catalytic particle size effect" significantly influences the activity and selectivity of Cu catalysts.[13,36,37] In this work, the Cu nanoparticles ranged from sub-2 to 100 nm by tuning the pyridyl content in the supporting GDY materials. In particular, **Py-GDY-Cu** has pushed the Cu particle size to a sub-2 nm level, where the quantum effect, also known as the "catalytic finite-size effect", becomes noticeable.[38] With the three supported Cu catalysts in hand, we surveyed their performance in the electrochemical CO_2 reduction reaction. The experiments were performed using a flow cell reactor, where a CO_2 stream and the commonly used 1.0 M KOH aqueous electrolyte were fed separately into the

2192 | *Inorg. Chem. Front.*, 2023, **10**, 2189–2196

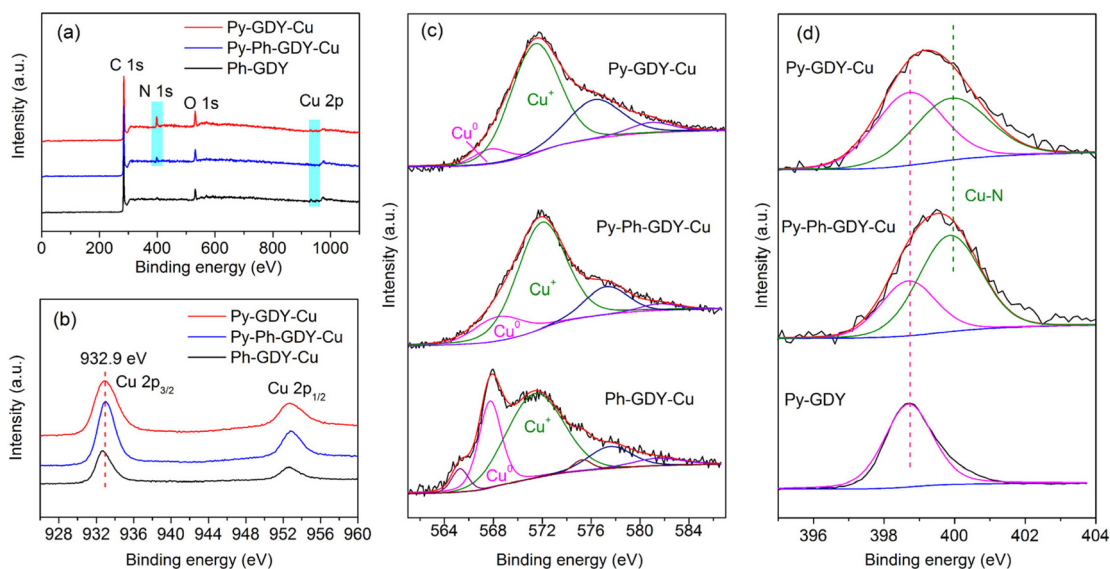This journal is © the Partner Organisations 2023

Fig. 4 (a) XPS spectra, (b) Cu 2p spectra, (c) Cu LMM Auger spectra of **Py-GDY-Cu**, **Py-Ph-GDY-Cu**, and **Ph-GDY-Cu**. (d) N 1s spectra of **Py-GDY-Cu**, **Py-Ph-GDY-Cu** and **Py-GDY**.

electrochemical cell through the two sides of the gas-diffusing electrode. Before the electrolysis experiments, electrochemical conditioning was applied for all three catalysts by cyclic voltammetry scanning from 0.5 V to −0.5 V vs. RHE for 60 cycles. After that, steady-state chronoamperometry measurements were conducted to evaluate the products of CO_2 reduction.

As shown in Fig. 5a–c, the electrolysis products consist of CO, CH_4, HCOOH, C_2H_4, CH_3CH_2OH, CH_3COOH, and H_2. The faradaic efficiency (FE) of CO decreased with applying more negative potentials due to the conversion of CO into other

hydrocarbons.[39] **Ph-GDY-Cu** showed a higher FE of C2 products (C_2H_4, CH_3CH_2OH, CH_3COOH) than **Py-Ph-GDY-Cu** and **Py-GDY-Cu** at all the applied potentials from −0.8 to −1.2 V vs. RHE, as shown in Fig. S18.† The highest FE of 31% for C2 products was achieved by **Ph-GDY-Cu** at −1.0 V vs. RHE. The highest FEs of C2 products for **Py-Ph-GDY-Cu** and **Py-GDY-Cu** were 23% and 21% at −0.8 V vs. RHE. As expected, the selectivity of C2 products increases as the size of the Cu particles increases because the large Cu particles favor the dimerization of *CO.[13] CH_4 dominates the products under most of the
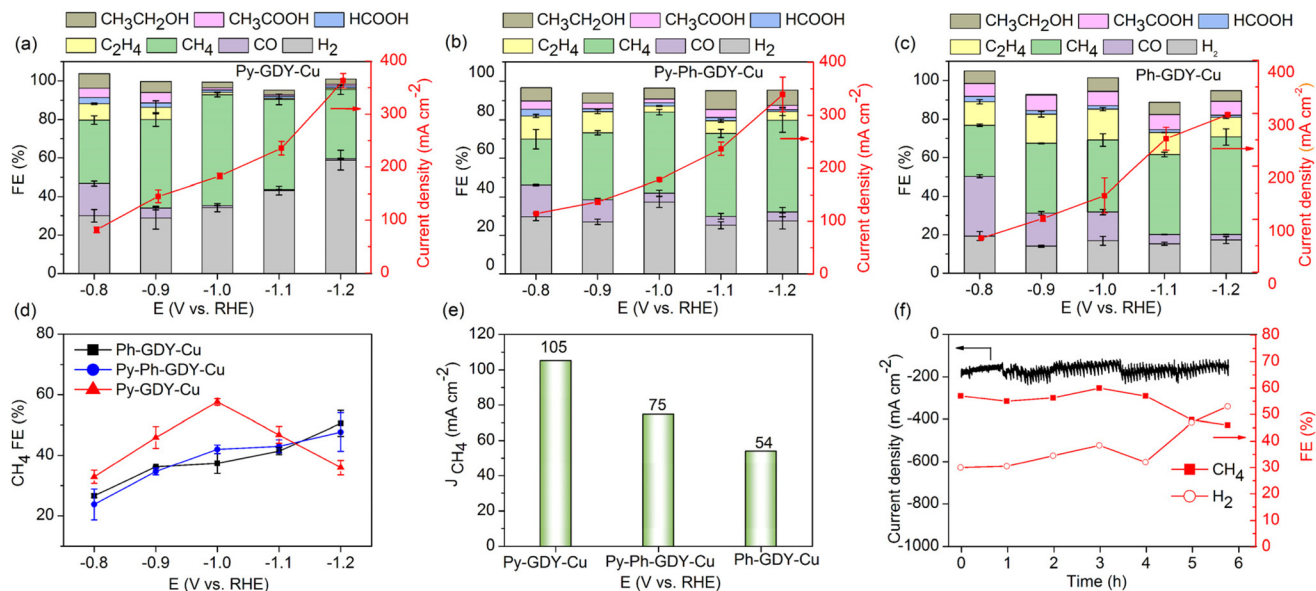

Fig. 5 CO_2 electroreduction performances of (a) **Py-GDY-Cu**, (b) **Py-Ph-GDY-Cu**, (c) **Ph-GDY-Cu** in 1.0 M KOH. (d) FE of CH_4 at −0.8 V to −1.2 V vs. RHE. (e) Partial current density of CH_4 at −1.0 V vs. RHE. (f) Stability test of **Py-GDY-Cu** and the FE of CH_4, H_2 measured every 1 h at −1.0 V vs. RHE.

This journal is © the Partner Organisations 2023

Inorg. Chem. Front., 2023, **10**, 2189–2196 | **2193**

tested potentials. As shown in Fig. 5a, **Py-GDY-Cu** leads to a higher selectivity of CH_4 than **Py-Ph-GDY-Cu** and **Ph-GDY-Cu** from −0.8 V to −1.1 V *vs.* RHE. The highest FE of CH_4 reaches 58% for **Py-GDY-Cu** at −1.0 V *vs.* RHE, while **Py-Ph-GDY-Cu** and **Ph-GDY-Cu** show CH_4 FEs of 42% and 37% at the same potential. On the other hand, **Py-Ph-GDY-Cu** and **Ph-GDY-Cu** show increased selectivity toward CH_4 with applying more negative potentials; this is due to the increased *H coverage and decreased *CO coverage at more cathodic potentials, which suppresses the generation of C2 products and facilitates the production of CH_4.[40,41] The CH_4 selectivity of **Py-Ph-GDY-Cu** and **Ph-GDY-Cu** at −1.2 V *vs.* RHE is still slightly lower than that of **Py-GDY-Cu** at −1.0 V *vs.* RHE. In contrast, **Py-GDY-Cu** displays decreased FE of CH_4 and increased FE of H_2 at −1.1 V and −1.2 V *vs.* RHE, which is very likely caused by the fact that **Py-GDY-Cu** is more hydrophilic than the other two catalysts, as indicated by their water contact angles in Fig. S19.† At −1.0 V *vs.* RHE, the partial current densities of CH_4 (Fig. 5e) were 105 mA cm^{-2}, 75 mA cm^{-2}, and 54 mA cm^{-2} for **Py-GDY-Cu**, **Py-Ph-GDY-Cu**, and **Ph-GDY-Cu**, respectively. Previous studies revealed that Cu$^+$ species could promote the generation of C2 products[42,43] while small-size Cu catalysts, such as sub-nanometric Cu clusters, favor the production of CH_4.[13,36] Which factor dictates the production selectivity of **Py-GDY-Cu**, **Py-Ph-GDY-Cu** and **Ph-GDY-Cu**? In our case, **Py-GDY-Cu** with the largest content of Cu$^+$ among these three samples displayed the highest CH_4 selectivity. Therefore, the product selectivity for our catalysts is not controlled by the Cu oxidation state. In contrast, the size effect could reasonably explain the product selectivity. Small Cu nanoclusters on **Py-GDY-Cu** prefer producing CH_4 over larger Cu aggregates on **Py-Ph-GDY-Cu** and **Ph-GDY-Cu**, in line with the previous works.[13,36]

The stability of **Py-GDY-Cu** was examined at the potential of −1.0 V *vs.* RHE in the 1.0 M KOH electrolyte. In Fig. 5f, no evident decay in the current density is observed after 6 h electrolysis, although some fluctuations exist during the test. The FE of CH_4 is 57% at the beginning and declines to 46% within 6 h, while the FE of H_2 increases from 30% to 53%, as shown in Fig. 5f. The change in FE is mainly caused by the flooding of the gas diffusing layer and the salt accumulation in the gas chamber during the electrolysis.[44] The structure of **Py-GDY-Cu** after 6 h electrolysis was characterized by TEM and XRD. As shown in Fig. S20,† no XRD peaks of Cu or CuO are found, and only the peaks ascribed to $KHCO_3$ appear. The aberration-corrected HAADF-STEM image (Fig. S21†) shows Cu nanoclusters retained on the surface of **Py-GDY-Cu**. These results indicate good stability of Cu nanoclusters on **Py-GDY** toward the electrochemical reduction of CO_2.

Conclusions

In summary, we have prepared a pyridyl-containing graphdiyne, **Py-GDY**, with evenly distributed pyridyl groups and uniform pores on the conjugated networks. The abundant pyridyl groups and porous structure of **Py-GDY** provide coordinating sites for anchoring metal atoms, and **Py-GDY-Cu** with sub-2 nm ultrasmall Cu clusters is realized using this novel supporting material. **Py-Ph-GDY-Cu** with decreased content of pyridyl groups possesses both Cu nanoclusters and nanoparticles (about 10 nm). For **Ph-GDY-Cu**, larger and uneven Cu nanoparticles are present. These results indicate the importance of pyridyl groups to restrict the aggregation of Cu and to facilitate the generation of Cu nanoclusters. Regarding the electrochemical reduction of CO_2, **Py-GDY-Cu** exhibits the highest FE of 58% for CH_4 at −1.0 V *vs.* RHE in 1.0 M KOH, which is more significant than the highest CH_4 FE obtained at −1.2 V *vs.* RHE by **Py-Ph-GDY-Cu** and **Ph-GDY-Cu**. The partial current densities of CH_4 at −1.0 V *vs.* RHE were 105 mA cm^{-2}, 75 mA cm^{-2}, and 54 mA cm^{-2} for **Py-GDY-Cu**, **Py-Ph-GDY-Cu** and **Ph-GDY-Cu**, respectively. The enhanced selectivity of CH_4 for **Py-GDY-Cu** is attributed to the small sizes of Cu nanoclusters stabilized by the pyridyl groups. Notably, the sub-2 nm ultrasmall Cu clusters of **Py-GDY-Cu** do not aggregate into large nanoparticles during CO_2 reduction. Overall, the precise installation of pyridyl groups into carbon-rich materials has been successfully illustrated by taking advantage of the bottom-up wet chemistry synthesis method of graphdiynes. The strong coordination pyridyl groups play a significant role in stabilizing ultrasmall Cu nanoclusters. Our strategy paves the way for synthesizing well-defined nitrogen-containing carbon materials and lays a foundation for the synthesis of ultrasmall metal nanoclusters.

Author contributions

L. D. conceived the project and designed the experiments. H. D. carried out the experiments and the electrochemical measurements. H. Z., T. S., L. G., C. H., contributed to TEM characterization. S. W., H. L., and H. X. contributed to the synthesis of several compounds and the Raman characterization. H. D., H. Z., and L. D. wrote the manuscript. All authors commented on the manuscript.

Conflicts of interest

There are no conflicts to declare.

Acknowledgements

2194 | *Inorg. Chem. Front.*, 2023, **10**, 2189–2196

This journal is © the Partner Organisations 2023

Notes and references

1 Y. Wang, H. Su, Y. He, L. Li, S. Zhu, H. Shen, P. Xie, X. Fu, G. Zhou, C. Feng, D. Zhao, F. Xiao, X. Zhu, Y. Zeng, M. Shao, S. Chen, G. Wu, J. Zeng and C. Wang, Advanced electrocatalysts with single-metal-atom active sites, *Chem. Rev.*, 2020, **120**, 12217–12314.

2 L. Liu and A. Corma, Metal catalysts for heterogeneous catalysis: from single atoms to nanoclusters and nanoparticles, *Chem. Rev.*, 2018, **118**, 4981–5079.

3 Z. Li, S. Ji, Y. Liu, X. Cao, S. Tian, Y. Chen, Z. Niu and Y. Li, Well-defined materials for heterogeneous catalysis: From nanoparticles to isolated single-atom sites, *Chem. Rev.*, 2020, **120**, 623–682.

4 A. Han, B. Wang, A. Kumar, Y. Qin, J. Jin, X. Wang, C. Yang, B. Dong, Y. Jia, J. Liu and X. Sun, Recent advances for MOF-derived carbon-supported single-atom catalysts, *Small Methods*, 2019, **3**, 1800471.

5 N. M. Julkapli and S. Bagheri, Graphene supported heterogeneous catalysts: An overview, *Int. J. Hydrogen Energy*, 2015, **40**, 948–979.

6 C.-L. Yang, L.-N. Wang, P. Yin, J. Liu, M.-X. Chen, Q.-Q. Yan, Z.-S. Wang, S.-L. Xu, S.-Q. Chu, C. Cui, H. Ju, J. Zhu, Y. Lin, J. Shui and H.-W. Liang, Sulfur-anchoring synthesis of platinum intermetallic nanoparticle catalysts for fuel cells, *Science*, 2021, **374**, 459–464.

7 L.-P. Yuan, T. Tang, J.-S. Hu and L.-J. Wan, Confinement strategies for precise synthesis of efficient electrocatalysts from the macroscopic to the atomic level, *Acc. Mater. Res.*, 2021, **2**, 907–919.

8 I. C. Gerber and P. Serp, A theory/experience description of support effects in carbon-supported catalysts, *Chem. Rev.*, 2020, **120**, 1250–1349.

9 D. Guo, R. Shibuya, C. Akiba, S. Saji, T. Kondo and J. Nakamura, Active sites of nitrogen-doped carbon materials for oxygen reduction reaction clarified using model catalysts, *Science*, 2016, **351**, 361–365.

10 S. Chen, T. Luo, X. Li, K. Chen, J. Fu, K. Liu, C. Cai, Q. Wang, H. Li, Y. Chen, C. Ma, L. Zhu, Y.-R. Lu, T.-S. Chan, M. Zhu, E. Cortés and M. Liu, Identification of the highly active Co–N_4 coordination motif for selective oxygen reduction to hydrogen peroxide, *J. Am. Chem. Soc.*, 2022, **144**, 14505–14516.

11 G. Li, Y. Li, H. Liu, Y. Guo, Y. Li and D. Zhu, Architecture of graphdiyne nanoscale films, *Chem. Commun.*, 2010, **46**, 3256–3258.

12 L. Hui, Y. Xue, H. Yu, Y. Liu, Y. Fang, C. Xing, B. Huang and Y. Li, Highly efficient and selective generation of ammonia and hydrogen on a graphdiyne-based catalyst, *J. Am. Chem. Soc.*, 2019, **141**, 10677–10683.

13 W. Rong, H. Zou, W. Zang, S. Xi, S. Wei, B. Long, J. Hu, Y. Ji and L. Duan, Size-dependent activity and selectivity of atomic-level Cu nanoclusters during CO/CO_2 electroreduction, *Angew. Chem., Int. Ed.*, 2020, **60**, 466–472.

14 H. Zou, W. Rong, S. Wei, Y. Ji and L. Duan, Regulating kinetics and thermodynamics of electrochemical nitrogen reduction with metal single-atom catalysts in a pressurized electrolyser, *Proc. Natl. Acad. Sci. U. S. A.*, 2020, **117**, 29462–29468.

15 Y. Xue, B. Huang, Y. Yi, Y. Guo, Z. Zuo, Y. Li, Z. Jia, H. Liu and Y. Li, Anchoring zero valence single atoms of nickel and iron on graphdiyne for hydrogen evolution, *Nat. Commun.*, 2018, **9**, 1460.

16 G. Shi, Y. Xie, L. Du, X. Fu, X. Chen, W. Xie, T.-B. Lu, M. Yuan and M. Wang, Constructing Cu–C bonds in a graphdiyne-regulated Cu single-atom electrocatalyst for CO_2 reduction to CH_4, *Angew. Chem., Int. Ed.*, 2022, **61**, e202203569.

17 X.-P. Yin, S.-F. Tang, C. Zhang, H.-J. Wang, R. Si, X.-L. Lu and T.-B. Lu, Graphdiyne-based Pd single-atom catalyst for semihydrogenation of alkynes to alkenes with high selectivity and conversion under mild conditions, *J. Mater. Chem. A*, 2020, **8**, 20925–20930.

18 H. Yu, Y. Xue, B. Huang, L. Hui, C. Zhang, Y. Fang, Y. Liu, Y. Zhao, Y. Li, H. Liu and Y. Li, Ultrathin nanosheet of graphdiyne-supported palladium atom catalyst for efficient hydrogen production, *iScience*, 2019, **11**, 31–41.

19 X. P. Yin, H. J. Wang, S. F. Tang, X. L. Lu, M. Shu, R. Si and T. B. Lu, Engineering the coordination environment of single-atom platinum anchored on graphdiyne for optimizing electrocatalytic hydrogen evolution, *Angew. Chem., Int. Ed.*, 2018, **57**, 9382–9386.

20 H. Yu, L. Hui, Y. Xue, Y. Liu, Y. Fang, C. Xing, C. Zhang, D. Zhang, X. Chen, Y. Du, Z. Wang, Y. Gao, B. Huang and Y. Li, 2D graphdiyne loading ruthenium atoms for high efficiency water splitting, *Nano Energy*, 2020, **72**, 104667.

21 Y. Yao, Y. Zhu, C. Pan, C. Wang, S. Hu, W. Xiao, X. Chi, Y. Fang, J. Yang, H. Deng, S. Xiao, J. Li, Z. Luo and Y. Guo, Interfacial sp C–O–Mo hybridization originated high-current density hydrogen evolution, *J. Am. Chem. Soc.*, 2021, **143**, 8720–8730.

22 C. Pan, C. Wang, X. Zhao, P. Xu, F. Mao, J. Yang, Y. Zhu, R. Yu, S. Xiao, Y. Fang, H. Deng, Z. Luo, J. Wu, J. Li, S. Liu, S. Xiao, L. Zhang and Y. Guo, Neighboring sp-hybridized carbon participated molecular oxygen activation on the interface of sub-nanocluster CuO/graphdiyne, *J. Am. Chem. Soc.*, 2022, **144**, 4942–4951.

23 Z. Wang, Z. Zheng, Y. Xue, F. He and Y. Li, Acidic water oxidation on quantum dots of IrO_x/graphdiyne, *Adv. Energy Mater.*, 2021, **11**, 2101138.

24 N. Wang, X. Li, Z. Tu, F. Zhao, J. He, Z. Guan, C. Huang, Y. Yi and Y. Li, Synthesis and electronic structure of boron-graphdiyne with an sp-hybridized carbon skeleton and its application in sodium storage, *Angew. Chem., Int. Ed.*, 2018, **57**, 3968–3973.

25 L. Gao, X. Ge, Z. Zuo, F. Wang, X. Liu, M. Lv, S. Shi, L. Xu, T. Liu, Q. Zhou, X. Ye and S. Xiao, High quality pyrazino-quinoxaline-based graphdiyne for efficient gradient storage of lithium ions, *Nano Lett.*, 2020, **20**, 7333–7341.

26 J. He, N. Wang, Z. Yang, X. Shen, K. Wang, C. Huang, Y. Yi, Z. Tu and Y. Li, Fluoride graphdiyne as a free-standing electrode displaying ultra-stable and extraordinary high Li storage performance, *Energy Environ. Sci.*, 2018, **11**, 2893–2903.

This journal is © the Partner Organisations 2023

Inorg. Chem. Front., 2023, **10**, 2189–2196 | **2195**

27 Q. Pan, S. Chen, C. Wu, Z. Zhang, Z. Li and Y. Zhao, Sulfur-rich graphdiyne-containing electrochemical active tetra-thiafulvalene for highly efficient lithium storage application, *ACS Appl. Mater. Interfaces*, 2019, **11**, 46070–46076.

28 N. Wang, J. He, Z. Tu, Z. Yang, F. Zhao, X. Li, C. Huang, K. Wang, T. Jiu, Y. Yi and Y. Li, Synthesis of chlorine-substituted graphdiyne and applications for lithium-ion storage, *Angew. Chem.*, 2017, **129**, 10740–10745.

29 Z. Zhang, C. Wu, Q. Pan, F. Shao, Q. Sun, S. Chen, Z. Li and Y. Zhao, Interfacial synthesis of crystalline two-dimensional cyano-graphdiyne, *Chem. Commun.*, 2020, **56**, 3210–3213.

30 N. Elgrishi, M. B. Chambers, X. Wang and M. Fontecave, Molecular polypyridine-based metal complexes as catalysts for the reduction of CO_2, *Chem. Soc. Rev.*, 2017, **46**, 761–796.

31 R. Matsuoka, R. Toyoda, R. Shiotsuki, N. Fukui, K. Wada, H. Maeda, R. Sakamoto, S. Sasaki, H. Masunaga, K. Nagashio and H. Nishihara, Expansion of the graphdiyne family: A triphenylene-cored analogue, *ACS Appl. Mater. Interfaces*, 2019, **11**, 2730–2733.

32 W. Zhou, H. Shen, C. Wu, Z. Tu, F. He, Y. Gu, Y. Xue, Y. Zhao, Y. Yi, Y. Li and Y. Li, Direct synthesis of crystalline graphdiyne analogue based on supramolecular interactions, *J. Am. Chem. Soc.*, 2019, **141**, 48–52.

33 D.-L. Meng, M.-D. Zhang, D.-H. Si, M.-J. Mao, Y. Hou, Y.-B. Huang and R. Cao, Highly selective tandem electroreduction of CO_2 to ethylene over atomically isolated nickel–nitrogen site/copper nanoparticle catalysts, *Angew. Chem., Int. Ed.*, 2021, **60**, 25485–25492.

34 I. Platzman, R. Brener, H. Haick and R. Tannenbaum, Oxidation of polycrystalline copper thin films at ambient conditions, *J. Phys. Chem. C*, 2008, **112**, 1101–1108.

35 S. Nitopi, E. Bertheussen, S. B. Scott, X. Liu, A. K. Engstfeld, S. Horch, B. Seger, I. E. L. Stephens, K. Chan, C. Hahn, J. K. Norskov, T. F. Jaramillo and I. Chorkendorff, Progress and perspectives of electrochemical CO_2 reduction on copper in aqueous electrolyte, *Chem. Rev.*, 2019, **119**, 7610–7672.

36 Q. Hu, Z. Han, X. Wang, G. Li, Z. Wang, X. Huang, H. Yang, X. Ren, Q. Zhang, J. Liu and C. He, Facile synthesis of sub-nanometric copper clusters by double confinement enables selective reduction of carbon dioxide to methane, *Angew. Chem., Int. Ed.*, 2020, **59**, 19054–19059.

37 R. Reske, H. Mistry, F. Behafarid, B. Roldan Cuenya and P. Strasser, Particle size effects in the catalytic electroreduction of CO_2 on Cu nanoparticles, *J. Am. Chem. Soc.*, 2014, **136**, 6978–6986.

38 L. Li, A. H. Larsen, N. A. Romero, V. A. Morozov, C. Glinsvad, F. Abild-Pedersen, J. Greeley, K. W. Jacobsen and J. K. Nørskov, Investigation of catalytic finite-size-effects of platinum metal clusters, *J. Phys. Chem. Lett.*, 2013, **4**, 222–226.

39 A. Wuttig, C. Liu, Q. Peng, M. Yaguchi, C. H. Hendon, K. Motobayashi, S. Ye, M. Osawa and Y. Surendranath, Tracking a common surface-bound intermediate during CO_2-to-fuels catalysis, *ACS Cent. Sci.*, 2016, **2**, 522–528.

40 Y. Huang, A. D. Handoko, P. Hirunsit and B. S. Yeo, Electrochemical reduction of CO_2 using copper single-crystal surfaces: Effects of CO* coverage on the selective formation of ethylene, *ACS Catal.*, 2017, **7**, 1749–1756.

41 X. Liu, P. Schlexer, J. Xiao, Y. Ji, L. Wang, R. B. Sandberg, M. Tang, K. S. Brown, H. Peng, S. Ringe, C. Hahn, T. F. Jaramillo, J. K. Nørskov and K. Chan, PH effects on the electrochemical reduction of CO_2 towards C_2 products on stepped copper, *Nat. Commun.*, 2019, **10**, 32.

42 Y. Zhou, F. Che, M. Liu, C. Zou, Z. Liang, P. De Luna, H. Yuan, J. Li, Z. Wang, H. Xie, H. Li, P. Chen, E. Bladt, R. Quintero-Bermudez, T.-K. Sham, S. Bals, J. Hofkens, D. Sinton, G. Chen and E. H. Sargent, Dopant-induced electron localization drives CO_2 reduction to C2 hydrocarbons, *Nat. Chem.*, 2018, **10**, 974–980.

43 P.-P. Yang, X.-L. Zhang, F.-Y. Gao, Y.-R. Zheng, Z.-Z. Niu, X. Yu, R. Liu, Z.-Z. Wu, S. Qin, L.-P. Chi, Y. Duan, T. Ma, X.-S. Zheng, J.-F. Zhu, H.-J. Wang, M.-R. Gao and S.-H. Yu, Protecting copper oxidation state via intermediate confinement for selective CO_2 electroreduction to C_{2+} fuels, *J. Am. Chem. Soc.*, 2020, **142**, 6400–6408.

44 W. Ma, X. He, W. Wang, S. Xie, Q. Zhang and Y. Wang, Electrocatalytic reduction of CO_2 and CO to multi-carbon compounds over Cu-based catalysts, *Chem. Soc. Rev.*, 2021, **50**, 12897–12914.